Photoelectrochemical performance of birnessite films and photoelectrocatalytic activity toward oxidation of phenol

Huiqin Zhang[1],[**], Hongrui Ding[1],[**], Xin Wang[2], Cuiping Zeng[1], Anhuai Lu[1],[*], Yan Li[1], Changqiu Wang[1]

1. *The Key Laboratory of Orogenic Belts and Crustal Evolution, School of Earth and Space Sciences, Peking University, Beijing 100871, China.*
E-mails: hqzhang_pku@163.com (Huiqin Zhang), dhr_100@163.com (Hongrui Ding)
2. *Institutes of Science and Development, Chinese Academy of Sciences, Beijing 100190, China*

ARTICLE INFO

ABSTRACT

Birnessite films on fluorine-doped tin oxide (FTO) coated glass were prepared by cathodic reduction of aqueous $KMnO_4$. The deposited birnessite films were characterized with X-ray diffraction, Raman spectroscopy, scanning electron microscopy and atomic force microscopy. The photoelectrochemical activity of birnessite films was investigated and a remarkable photocurrent in response to visible light was observed in the presence of phenol, resulting from localized manganese *d–d* transitions. Based on this result, the photoelectrocatalytic oxidation of phenol was investigated. Compared with phenol degradation by the electrochemical oxidation process or photocatalysis separately, a synergetic photoelectrocatalytic degradation effect was observed in the presence of the birnessite film coated FTO electrode. Photoelectrocatalytic degradation ratios were influenced by film thickness and initial phenol concentrations. Phenol degradation with the thinnest birnessite film and initial phenol concentration of 10 mg/L showed the highest efficiency of 91.4% after 8 hr. Meanwhile, the kinetics of phenol removal was fit well by the pseudofirst-order kinetic model.

© 2016 The Research Center for Eco-Environmental Sciences, Chinese Academy of Sciences. Published by Elsevier B.V.

Introduction

Photoelectrocatalytic (PEC) oxidation in the presence of semiconductor photoelectrodes has been proven to be an efficient process that can be used for degradation of various organic pollutants, such as dyes (Zhang et al., 2007; Yang et al., 2005; Shinde et al., 2012), pesticides (Philippidis et al., 2009), aromatics (Chen et al., 2009; Yang et al., 2006; Neumann-Spallart et al., 2013), and so on. In most of these cases, an electrode coated with TiO_2 film was used as a photoanode. However, the wide bandgap of TiO_2 (about 3.2 eV) results in a lack of absorption in the visible portion of the solar light spectrum and limits the application of TiO_2. In order to increase the photocatalytic activity under visible irradiation, extensive studies have focused on doping metals (Fe, Cu, Cr, *etc.*) or non-metals (carbon and nitrogen) into TiO_2 to narrow the bandgap of TiO_2 (Zhang and Lei, 2008; Hua et al., 2015; Yang et al., 2014; Chen et al., 2009; Lan et al., 2013). As an alternative, some novel photocatalysts with response to visible light, such as Fe_2O_3, WO_3 and metal-free g-C_3N_4, have been developed (Zhang et al., 2010; Hepel and Hazelton, 2005; Cheng et al., 2007; Shinde et al., 2013, 2016). Fe_2O_3, WO_3 and g-C_3N_4 have narrow bandgaps of about 2.0–2.2 eV, 2.5 eV and 2.7 eV and can thus absorb part of the solar spectrum (Cesar et al., 2006; Hu et al., 2008; Spichiger-Ulmann and Augustynski, 1983; Shinde et al., 2016).

---

  * *Corresponding author*. E-mail: ahlu@pku.edu.cn (Anhuai Lu).
 ** The authors contributed equally to this article.

Birnessite is a naturally occurring phyllomanganate consisting of edge-sharing sheets of MnO_6 octahedra with an interlayer distance at about 0.7 nm, and hydrated alkali metal cations (Na^+, K^+, *etc.*) in the interlayers that compensate the small overall negative charge. With a bandgap energy of 1.8–2.1 eV (Sherman, 2005; Pinaud et al., 2011; Hsu et al., 2012), birnessite is also an important photoactive material that can adsorb part of solar spectrum up to *ca.*, 600 nm (Hsu et al., 2012). Over the last decades, catalytic activity of birnessite has been observed in the oxidation of indigo carmine (Zaied et al., 2011), benzene (Ye et al., 2014; Hou et al., 2014), phenolic compounds (Nakayama et al., 2010; Chien et al., 2008; Hardie et al., 2007), *etc.* However, leaching of the reduced Mn species may impede the catalytic reaction and have a negative effect on the recycling of the manganese dioxide. A PEC degradation process could avoid these problems, and usually has higher efficiency than photocatalytic processes (Yang et al., 2006; Kesselman et al., 1997). Recently, some researchers have reported the photoelectrochemical properties of functional manganese oxide used for water splitting to generate hydrogen. Sakai et al. (2005) first reported the observation of photocurrent generation by MnO_2 nanosheets on indium tin oxide under visible light irradiation in a nonaqueous electrolyte. Hsu et al. (2012) demonstrated that birnessite nanosheets delivered remarkable photocurrent in the presence of a hole scavenger. Nevertheless, the PEC behavior of birnessite has been less extensively studied than other transition metal oxides such as Fe_2O_3 and WO_3, especially the efficiency of PEC degradation of organic pollutants on MnO_2-electrodes under visible light irradiation, and there is still much work to do.

In this study, direct growth of birnessite films with a series of thicknesses on FTO-coated glass was carried out by cathodic reduction of aqueous MnO_4^- ions. The photocatalytic activity of birnessite films of different thickness was evaluated in the presence of phenol. The influence of bias potential, thickness of birnessite sheet and initial phenol concentrations on phenol degradation was considered. The results showed that birnessite exhibits favorable photocatalytic properties and has application potential for organic pollutant degradation.

1. Experimental

1.1. Sample preparation

The cathodic deposition of birnessite-type manganese oxide was performed in a three-electrode electrochemical cell at room temperature (Nakayama et al., 2012). A platinum sheet (1 cm × 1 cm) and a saturated calomel electrode (SCE) were used as the counter and reference electrodes, respectively. Fluorine-doped tin oxide (FTO) substrates on glass supports served as the working electrodes. Prior to electrodeposition, the electrode surface was cleaned by ethanol and distilled water ultrasonically for 30 min each. A solution with 2 mmol/L $KMnO_4$ and 50 mmol/L KCl acted as electrolyte for the electrodeposition. The exposed area of the working electrode was 2.5 × 2 cm^2. A potentio/galvanostat electrochemical workstation (CHI 760E) was used to maintain a constant potential of –0.05 V (vs. SCE)

during the deposition process. The film thickness was controlled by varying the delivered charge from 0.3 to 2.0 C.

1.2. Film characterization

X-ray diffraction (XRD) patterns were recorded using an X'Pert Pro MPD powder diffractometer (PANalytical B.V., Netherlands) with CuKα radiation (λ = 0.15406 nm). The instrument was operated at a tube voltage of 40 kV and a tube current of 40 mA. Intensities were measured at 2θ = 5°–70° with 0.017° two-theta steps and a count time of 0.3 sec per step.

The mineral micro-morphologies were observed using an FEI NanoSEM 430 Field Emission Gun scanning electron microscope (SEM) (FEI Corp., USA). The samples were mounted on an aluminum SEM stub via conductive tape and coated with gold using a Denton Desk II Gold Sputter Coater before SEM observations. The SEM was operated at an accelerating voltage of 10 kV.

Raman spectra were measured using a Renishaw inVia Reflex system (Renishaw, UK) equipped with a 532 nm laser and a 50× objective. To obtain a high signal-to-noise ratio, each Raman spectrum was the average of 12 successive scans obtained at a spectral resolution of 1 cm^{-1}. The frequency stability and accuracy of the apparatus were checked by recording the Raman spectrum of silicon.

Thickness measurements were performed using a Bruker Dimension ICON Atomic Force Microscope (AFM) (Bruker, USA). The film was partially lifted off the substrate using a scalpel and then laid on the sample stage with the boundary between birnessite-coated and uncoated regions beneath the AFM tip. Imaging was performed in ScanAsyst® mode over a range of 50 × 10 μm. Average step heights along the X-axis were obtained using the "step" feature in NanoScope_Analysis software. The height diagrams obtained for each image gave three stages corresponding to the average heights of substrate, coating and transition region. By subtracting the substrate height from the coating height, the film thickness was obtained.

1.3. Photoelectrochemical measurements and analytical method

Photoelectrochemical measurements were carried out with a set-up consisting of a 30 mL cylindrical quartz glass reactor, external simulated solar light (white LED lamp) and a three-electrode configuration. The initial volume of the working solution was 20 mL with different initial phenol concentrations. The pH of the solution was fixed at 6.0 using a Mettler Toledo pH meter. Ultrapure water (18 MΩ·cm) was used throughout the experiments. To maintain suitable solution conductivity, 0.1 mol/L Na_2SO_4 was chosen as the supporting electrolyte. The incident light was irradiated onto birnessite film electrodes from the back face through the quartz window. The intensity of radiation at the position of the sample was approximately 60 mW/cm^2. Cooling of the reactor was assured by means of air flow using an incorporated fan. A potential of 1.0 V (vs SCE) was applied in the photocurrent measurement and the phenol degradation process.

In the PEC phenol oxidation process, samples were collected from the reaction solution at regular time intervals to determine the residual concentration of phenol. Total organic carbon

(TOC) was measured by a TOC analyzer (multi N/C 3000, Analytik Jena AG, Germany). The phenol concentration was monitored with a Thermo Evolution 220 spectrophotometer (Thermo, USA). Phenol was analyzed by reacting with 4-aminoantipyrine in the presence of potassium ferricyanide to form a red complex, with maximum absorption at the wavelength of 510 nm (Chen et al., 1998). The efficiency of the phenol degradation was estimated by Eq. (1):

$$\text{Phenol degradation ratio} = (C_0 - C_t)/C_0 \times 100\% \qquad (1)$$

where C_0 (mg/L) and C_t (mg/L) are the phenol concentrations initially and at time t, respectively. The rate of phenol degradation can be described by a pseudo-first order model:
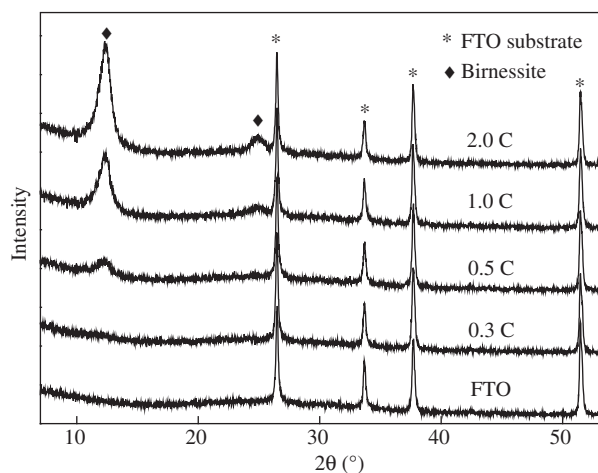
$$\ln(C_t/C_0) = -kt \qquad (2)$$

where k is the apparent rate constant for the PEC degradation reaction.

2. Results and discussion

2.1. Structural and optical characterization

The manganese mineral films deposited with the delivered charge of 0.3, 0.5, 1.0 and 2.0 C were characterized by XRD analysis (Fig. 1). Two diffraction peaks were observed at 12.3° and 24.8°, which were assigned to the (001) and (002) planes of the crystalline birnessite-type layered structure, where K$^+$ ions were accommodated between the MnO$_6$ layers. Data for $2\theta = 40$–70° are not shown in the figure as all peaks in this range were attributable to the FTO substrate. The strongest diffraction peaks were observed in the film deposited with the delivered charge of 2.0 C. With a decrease in the delivered charge, the diffraction peaks decreased in intensity. When the delivered charged was reduced to 0.3 C, the two peaks at 12.3° and 24.8° became indistinguishable, as the MnO$_2$ film was too thin to be detected by XRD.

Raman spectra of MnO$_2$ films showed three major vibrational features corresponding to birnessite, which could be recognized at 512, 576 and 635 cm^{-1} (Julien et al., 2003) (Fig. 2). The Raman band at 635 cm^{-1} could be attributed to the symmetric stretching vibration ν_2(Mn–O) of MnO$_6$ groups. The band located at 576 cm^{-1} was attributed to the ν_3(Mn–O) stretching vibration in the basal plane of MnO$_6$ sheets. The low wavenumber Raman features were associated with K–O vibrations (Julien et al., 2003). It should be noted that these vibrational features of the film with 0.3 C delivered charge were the same as for the others except for its lower intensity. From these results, the presence of birnessite-type MnO$_2$ with layered structure can be concluded.

The SEM images of the manganese minerals deposited on the FTO glass surface showed that the films with the delivered charge of 0.3, 0.5 and 1.0 C were composed of wrinkled thin sheets, and the thinnest films with the least delivered charge of 0.3 C had a more uneven morphology, which could expose a larger surface area to the electrolyte (Fig. 3). The film formed with the most delivered charge of 2.0 C had more layers and a more even morphology as a whole, whilst it had a lot of cracks. The thicknesses of the birnessite films were further measured using AFM (Appendix A Fig. S1), which gave the results of 178, 208, 219 and 338 nm corresponding to the delivered charge of 0.3, 0.5, 1.0 and 2.0 C. It was found that the flatness and thickness of birnessite films increased with increasing delivered charge, while the difference between films with delivered charges of 0.5 and 1.0 C was relatively smaller.

2.2. Electrochemical characterization

The photocurrent-time response of birnessite films was determined by amperometric i–t curves under a constant potential of 1.0 V. The optimal potential of 1.0 V was taken from previous studies on manganese oxides or TiO$_2$/Ti composite electrodes (Hsu et al., 2012; Bennani et al., 2014). All i–t curves were processed by subtracting the baselines (Fig. 4a). The positive photocurrents corresponded to a photo-oxidation process and
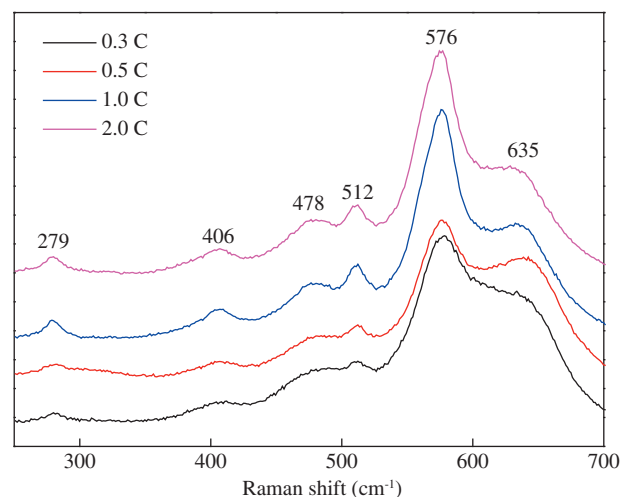

Fig. 1 – X-ray diffraction (XRD) patterns of manganese mineral films deposited with the delivered charges of 0.3, 0.5, 1.0 and 2.0 C.

Fig. 2 – Raman spectra of manganese mineral films deposited with the delivered charges of 0.3, 0.5, 1.0 and 2.0 C.
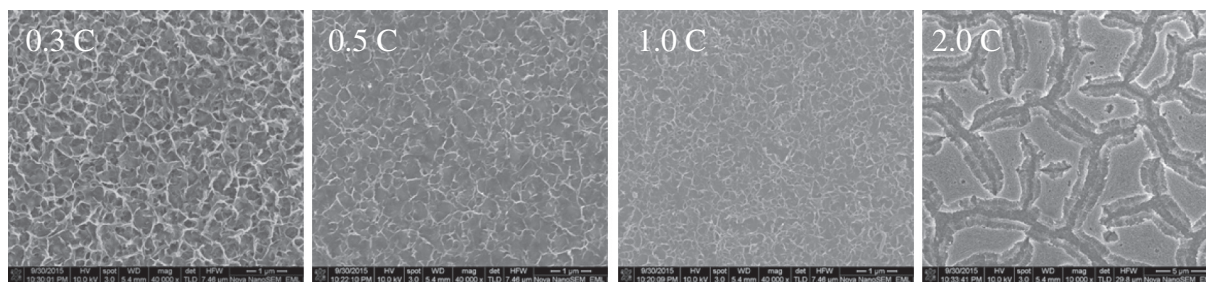
Fig. 3 – Scanning electron microscopy (SEM) images of the films deposited with the delivered charges of 0.3, 0.5, 1.0 and 2.0 C.

indicated that birnessite, as a photoanode, was an n-type semiconductor (Ohko, 1997; Sakai et al., 2005; Hsu et al., 2012). All photocurrents immediately increased when light was turned on, and rapidly went back to baseline when the light was off. But there still were some differences. During the time period when light was on, the photocurrent slightly increased. Birnessite with delivered charge of 0.3 and 0.5 C showed "flatter" patterns than samples prepared with delivered charge of 1.0 and 2.0 C. The photocurrent density decreased with the increase of the thickness of birnessite films. For the thick films, the recombination of photoelectron–hole pairs rather than charge transfer easily took place because of higher internal resistance. Meanwhile, the microstructure of the films may have an effect on the active sites available for the reaction with phenol, and the films with more uneven morphology had more active sites.

The effect of phenol concentration on the response of the birnessite film with the delivered charge of 0.5 C was investigated (Fig. 4b). The photocurrent in the presence of phenol was much higher than that without phenol. The photocurrent of birnessite involves a d–d transition under light illumination (Sakai et al., 2005; Kwon et al., 2008). Due to the low mobility of d electrons, migration of the excited carriers into the electrolyte is difficult and photogenerated pairs are likely to recombine (Sakai et al., 2005; Leland and Bard, 1987). With the presence of phenol in the electrolyte, photo-generated holes would be scavenged by phenol, suppressing the electron-hole recombination in birnessite. In addition, slower rise time was observed with the presence of phenol. The slower rising region corresponds to a long-time saturation conduction mechanism in the photocurrent generating processes, which was thought to be related to phenol adsorption on birnessite films (Wu et al., 2015). Comparative photocurrents in the presence of various phenol concentrations are also shown in Fig. 4b. In the concentration range of 0–40 mg/L, the photocurrent dramatically increased from 6.4 to 14.4 μA/cm^2. When the concentration increased to 100 and 200 mg/L, the photocurrent went up slightly to 15.6 and 16.2 μA/cm^2, respectively. It was assumed that the rate of the photochemical reaction was proportional to the surface concentration of photogenerated holes and electrons, and with the presence of a positive bias on semiconductor catalyst, the electrons flowed through the external circuit, so the photocurrent density should be analogous to the reaction rate. The Langmuir–Hinshelwood model was used to clarify the relation between the photocurrent and phenol concentrations (Turchi and Ollis, 1990; Hsu et al., 2012):

$$I_{ph} = AC_m/(C + BC_m) \tag{3}$$

where I_{ph} (μA/cm^2) and C_m (mg/L) are the photocurrent and phenol concentrations, while A, B and C are the constants. Rearrangement of Eq. (3) gives:
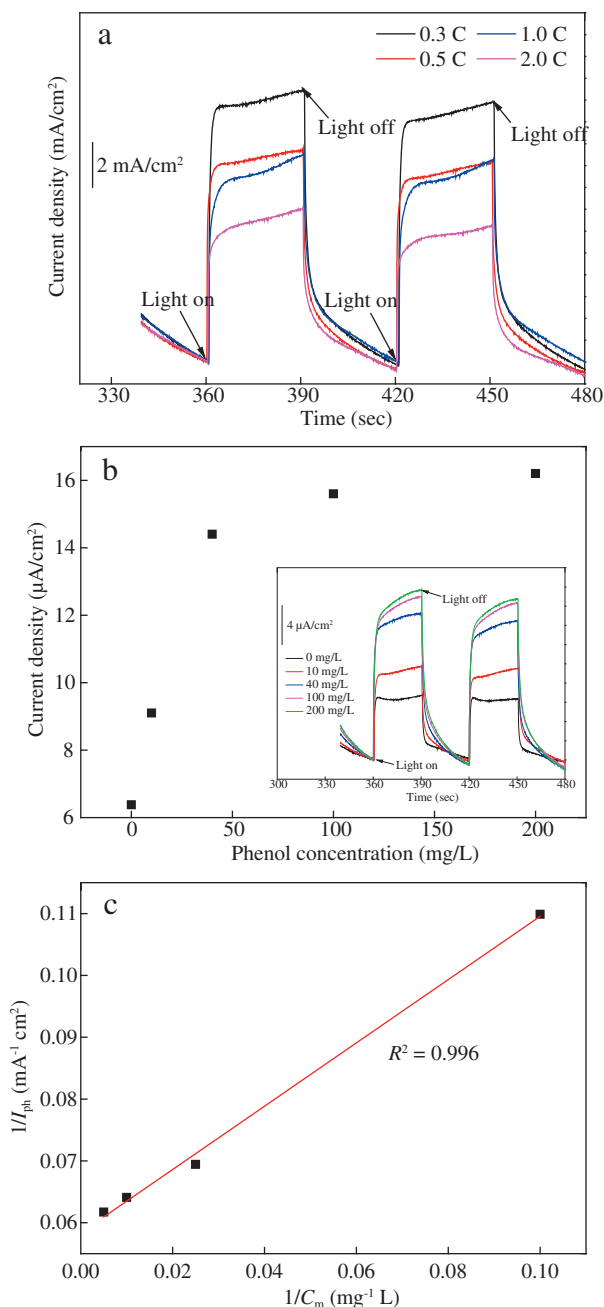
$$1/I_{ph} = A' + B'/C_m \tag{4}$$

where A' and B' are the constants. So in this study, as shown in Fig. 4c, the linear relationship between $1/I_{ph}$ and $1/C_m$ revealed that the relation between the photocurrent and phenol concentrations fit well to the Langmuir–Hinshelwood model.

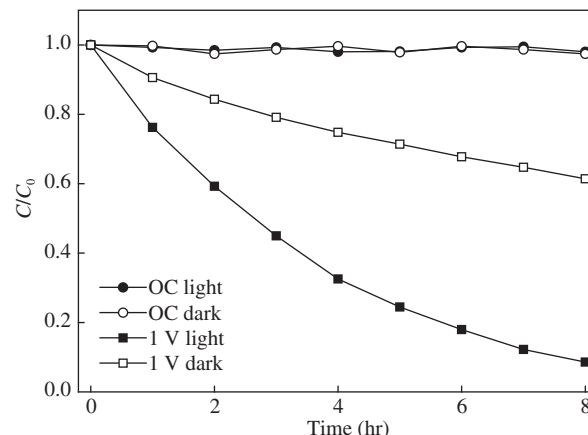### 2.3. Photoelectrocatalytic phenol degradation

The phenol degradation efficiencies at open circuit and a constant potential of 1.0 V were compared (Fig. 5). Without external potential, no obvious degradation was detected. It has been reported that phenol oxidation by manganese oxide usually occurs at pH <4 (Ukrainczyk, 1992). In our experiment, initial pH was fixed at 6.0, and direct oxidation of phenol was negligible. In addition, the irradiation did not promote phenol degradation, which means that direct photocatalysis did not take place in the process. With a constant potential of 1.0 V, the degradation ratio in the dark was 38.6%, attributed to electro-chemical phenol degradation. When the light irradiation was introduced, the degradation ratio was greatly enhanced (91.4%), indicating the presence of a synergistic effect between photo-chemical and electrochemical oxidation. When birnessite was illuminated by visible light, electrons in the valence band were excited to the conduction band and holes were generated in the valence band as shown in Fig. 6. Without external bias potential, as the conduction band of birnessite was too low, oxygen reduction or the photocatalytic degradation of pollutants could not take place. A schematic diagram of the PEC system is shown in Fig. 6. The external potential promoted the photoelectron to transfer to the electrode, avoiding the recombination of the photoelectron-hole pairs, and thus the phenol molecules adsorbed on the surface of the anode would be oxidized by photo-generated holes directly or by free radicals (Shinde et al., 2013; Cheng et al., 2007).

Fig. 4 – Photocurrent response of birnessite films of different thickness in the presence of 10 mg/L phenol (each line were processed to subtract the baseline) (a) and photocurrent response of birnessite films with the delivered charge of 0.5 C in presence of phenol of different initial concentrations (b) at an applied potential of 1.0 V; the plot of the reciprocal photocurrent as a function of the reciprocal phenol concentration (c).

Fig. 5 – Phenol degradation by birnessite film with the delivered charge of 0.3 C at open circuit (OC) and a constant potential of 1.0 V with and without light irradiation.

0.5, 1.0, 2.0 C) reached 91.4%, 83.1%, 80.6% and 67.2%, respectively. The results showed that thinner birnessite films had higher phenol degradation rates, which was similar to trend of the photocurrent. The kinetics of phenol removal with birnessite from thin to thick (delivered charge 0.3, 0.5, 1.0 and 2.0 C) fitted the pseudo first-order kinetic model well, with rate constants (k) of 0.305, 0.236, 0.198 and 0.136 hr^{-1} and R^2 values of 0.996, 0.981, 0.988 and 0.994, respectively (Table 1 and Fig. 7b). Comparing our result with a similar experiment using TiO_2 ($k = 0.216$), it is evident that birnessite had even higher activity in the degradation of phenol under visible light (Bennani et al., 2015).

The UV–Vis spectra of the phenol solution (initial concentration at 10 mg/L) in the range of 200–320 nm changed during the reaction with irradiation (Fig. 8). The maximum absorbance peak of phenol in aqueous solution was at 269 nm. In the course of the reaction, the phenol absorbance band became weak and finally disappeared after 8 hr. An absorption peak at 245 nm, typical for p-benzoquinone (Ukrainczyk, 1992; Drozd et al., 2014), appeared from 2 to 6 hr and finally the p-benzoquinone band became indistinguishable after 8 hr, indicating that p-benzoquinone might be an intermediate of PEC phenol

Fig. 6 – Schematic diagram of birnessite photoelectrocatalytic (PEC) system.
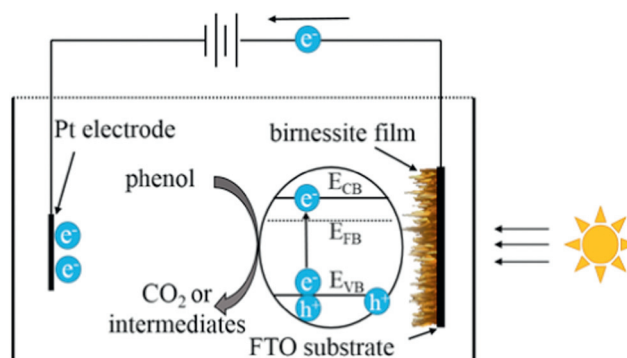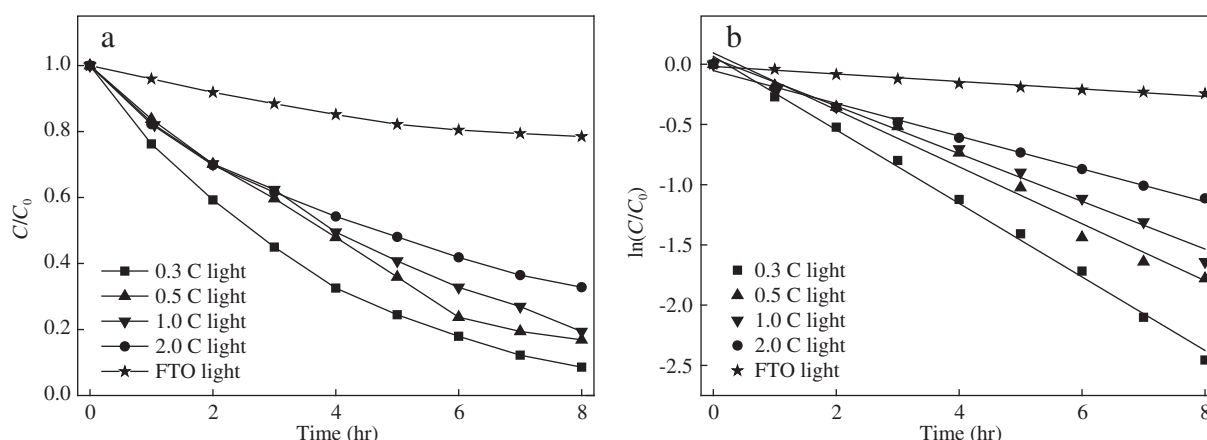
The FTO electrodes coated with birnessite films of different thicknesses showed different phenol degradation efficiency (Fig. 7a). With FTO itself, the degradation ratio in light was 21.5%. With birnessite on FTO, the degradation ratios were significantly enhanced. Phenol removal ratios with birnessite from thin to thick (corresponding to delivered charge of 0.3,

Fig. 7 – Kinetics curves and pseudo-first order kinetics plots of PEC phenol degradation on birnessite films of different thickness in presence of 10 mg/L phenol at a constant potential of 1.0 V with light irradiation.

degradation. Besides, the TOC values of samples before and after PEC oxidation were calculated to be 10.20 and 4.54 mg/L, respectively, corresponding to a TOC removal of about 55.5%. The results indicated that the majority of phenol was oxidized completely to CO_2, while some was oxidized incompletely to some intermediates.
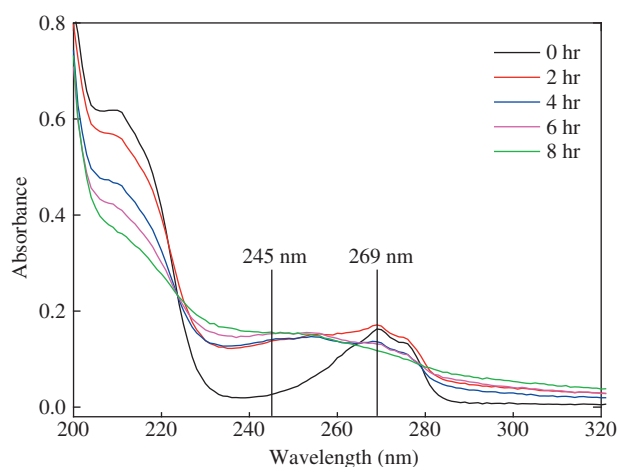
Phenol degradation for different initial concentrations is shown in Fig. 9 and Table 2. When the phenol concentration was 10, 40 and 100 mg/L, 91.4%, 38.2% and 14.0% phenol was degraded, respectively. The degradation ratio and the apparent rate constant (k) decreased as the initial concentration of phenol increased. To determine the efficiency of the PEC system with different concentrations, the net amount of phenol degraded for different initial phenol concentrations was calculated. The results showed that the net amount of phenol degraded (3.24 μmol) with initial concentration of 40 mg/L, was the highest among the three (Table 2). Meanwhile, the amount of phenol degraded slightly decreased to 3.10 μmol when the initial concentration was raised to 100 mg/L. The current was monitored over the course of the reaction (Appendix A Fig. S2). It was found that in the initial 14 min, the current for initial concentration of 100 mg/L was higher than that of 40 mg/L, which was in accordance with the result in Fig. 4b, then, it gradually dropped to the same level as that with initial concentration of 10 mg/L, lower than that with initial concentration of 40 mg/L. Then, after about

1.5 hr, all the currents became similar. In the initial stage, the photocurrent was kinetically controlled and was enhanced for higher phenol concentrations. Afterward, the catalytic active sites became rate-limiting for oxidization of phenol. At high concentrations of phenol, the adsorption of phenol molecules on the catalyst surface reached saturation so that the degradation rate did not increase any longer.

The stability of the birnessite film on FTO electrodes was investigated by repeating the phenol PEC degradation experiments at the bias potential of 1.0 V for 8 hr for five repeated cycles (Appendix A Table S1). The degradation efficiencies over 2–5 cycles remained stable in the range of 86%–90%, very close to that of the first cycle (91.4%), indicating that the birnessite film on the electrode was stable for at least 5 repeated degradation experiments. The film after PEC reaction was analyzed by Raman spectroscopy (Fig. 10), and three major vibrational features corresponding to birnessite at 512, 576 and 635 cm^{-1} were still observed, which confirmed that the birnessite phase was stable on the FTO electrode.

Table 1 – PEC kinetic rate constants and correlation coefficients of birnessite electrodes with different thickness at a constant potential of 1.0 V with light irradiation.

Charge delivered (C)	Thickness (nm)	First-order rate constant k (hr^{-1})	Correlation coefficient R^2	Phenol degradation ratio
0	0	0.031	0.967	21.7%
0.3	178	0.305	0.996	91.4%
0.5	208	0.236	0.981	83.1%
1.0	219	0.198	0.988	80.6%
2.0	338	0.136	0.994	67.2%

Fig. 8 – Time courses of phenol UV–vis absorption spectra in PEC degradation process at a constant potential of 1.0 V with light irradiation.
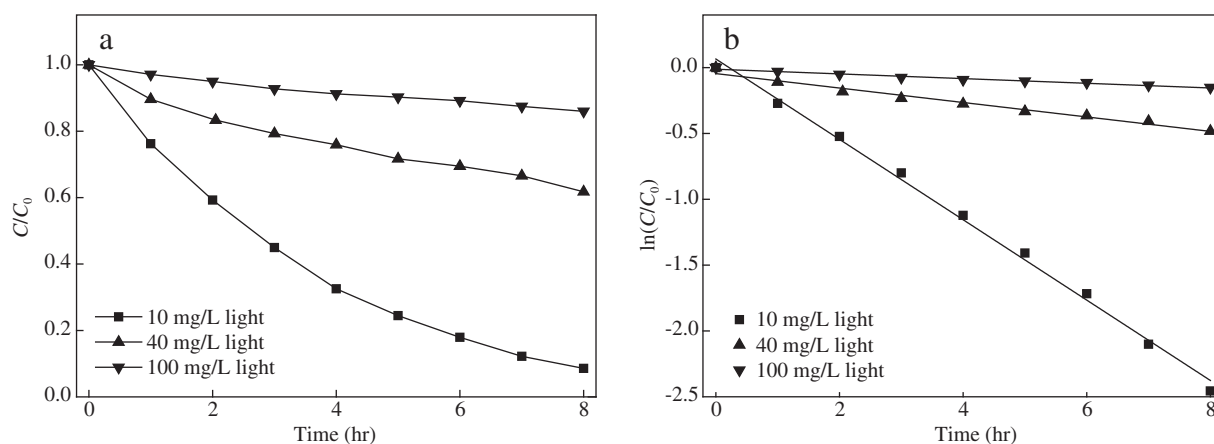
Fig. 9 – Kinetic curves and pseudo-first-order kinetics plots of PEC phenol degradation on birnessite film with the delivered charge of 0.3 C in the presence of phenol at different concentrations at a constant potential of 1.0 V with irradiation.

Table 2 – PEC kinetic rate constants and correlation coefficients of birnessite electrode in the presence of phenol of different initial concentrations at a constant potential of 1.0 V with irradiation.

Initial phenol concentration (mg/L)	First-order rate constant k (hr^{-1})	Correlation coefficient R^2	Phenol degradation ratio	Phenol degraded (μmol)
10	0.305	0.996	91.4%	1.97
40	0.055	0.974	38.2%	3.24
100	0.018	0.978	14.0%	3.10

The actual initial phenol concentrations were slightly different from the nominal concentrations, and the amount of phenol degraded was calculated according to the actual initial phenol concentration.

However, the intensity of the Raman features became weak. Meanwhile, it could be found by AFM (Appendix A Fig. S3) that the wrinkled thin sheets became looser. It is concluded that the phase structure of the film was stable, while the micro-structural features such as morphology and crystallinity may have undergone some changes.
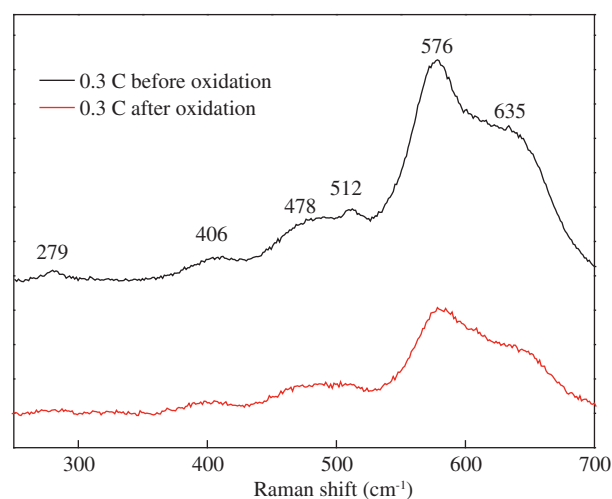

Fig. 10 – Raman spectra of birnessite deposited with the delivered charge of 0.3 C before and after PEC phenol oxidation.

3. Conclusions

Birnessite films were successfully synthesized on FTO-coated glass by cathodic reduction of aqueous KMnO$_4$. Remarkable photocurrents in response to visible light were observed in the presence of phenol, resulting from localized manganese d–d transitions. The intensity of the photocurrent was related to the thickness of the birnessite film and the concentration of phenol. Under visible irradiation and the bias potential of 1.0 V, birnessite showed PEC activity toward phenol. The degradation of phenol followed a pseudo-first-order kinetic model and was also influenced by the thickness of the birnessite film and the concentration of phenol. The degradation ratio and apparent rate constant decreased with an increase of the initial concentration of phenol or thickness of the birnessite film. The thinnest birnessite film, which resulted in more charge transfer, gave the highest phenol degradation efficiency of 91.4%, and remained stable after 5 repeated experiments. These results show that PEC oxidation using birnessite film electrodes could hold promise as a powerful tool for the degradation of hazardous organics in water.

Acknowledgments

Appendix A. Supplementary data

Supplementary data to this article can be found online at http://dx.doi.org/10.1016/j.jes.2016.04.009.

REFERENCES

Bennani, Y., Appel, P., Rietveld, L.C., 2015. Optimisation of parameters in a solar light-induced photoelectrocatalytic process with a TiO$_2$/Ti composite electrode prepared by paint-thermal decomposition. J. Photochem. Photobiol. A Chem. 305, 83–92.

Bennani, Y., El-Kalliny, A.S., Appel, P.W., Rietveld, L.C., 2014. Enhanced solar light photoelectrocatalytic activity in water by anatase-to-rutile TiO$_2$ transformation. J. Adv. Oxid. Technol. 17 (2), 285–296.

Cesar, I., Kay, A., Grätzel, M., 2006. Translucent thin film Fe$_2$O$_3$ photoanodes for efficient water splitting by sunlight: nanostructure-directing effect of Si-doping. J. Am. Chem. Soc. 128 (14), 4582–4583.

Chen, L., Huang, C., Ho, Y., Guo, W., Pan, T., 2009. Enhanced visible light-induced photoelectrocatalytic degradation of phenol by carbon nanotube-doped TiO$_2$ electrodes. Electrochim. Acta 54 (15), 3884–3891.

Chen, Y., Wang, S., Zhou, T., 1998. Spectrophotometric determination of trace phenol in water after preconcentration on an organic solvent–soluble membrane filter. Anal. Lett. 31 (7), 1233–1245.

Cheng, X.F., Leng, W.H., Liu, D.P., Zhang, J.Q., Cao, C.N., 2007. Enhanced photoelectrocatalytic performance of Zn-doped WO$_3$ photocatalysts for nitrite ions degradation under visible light. Chemosphere 68 (10), 1976–1984.

Chien, S.W.C., Chen, H.L., Wang, M.C., Seshaiah, K., 2008. Oxidative degradation and associated mineralization of R, hydroquinone and resorcinol catalyzed by birnessite. Chemosphere 74 (8), 1125–1133.

Drozd, D., Szczubiałka, K., Kumorek, M., Kepczynski, M., Nowakowska, M., 2014. Photoactive polymer-nanoclay hybrid photosensitizer for oxidation of phenol in aqueous media with the visible light. J. Photochem. Photobiol. A 288, 39–45.

Hardie, A.G., Dynes, J.J., Kozak, L.M., Huang, P.M., 2007. Influence of polyphenols on the integrated polyphenol-maillard reaction humification pathway as catalyzed by birnessite. Ann. Environ. Sci. 1, 91–110.

Hepel, M., Hazelton, S., 2005. Photoelectrocatalytic degradation of diazo dyes on nanostructured Wo3 electrodes. Electrochim. Acta 50 (25), 5278–5291.

Hou, J., Li, Y., Mao, M., Lu, R., Zhao, X., 2014. Tremendous effect of the morphology of birnessite-type manganese oxide nanostructures on catalytic activity. ACS Appl. Mater. Interfaces 6 (17), 14981–14987.

Hsu, Y.K., Chen, Y.C., Lin, Y.G., Chen, L.C., Chen, K.H., 2012. Birnessite-type manganese oxides nanosheets with hole acceptor assisted photoelectrochemical activity in response to visible light. J. Mater. Chem. 22 (6), 2733–2739.

Hu, Y.S., Kleiman-Shwarsctein, A., Forman, A.J., Hazen, D., Park, J.N., Mcfarland, E.W., 2008. Cheminform abstract: Pt-doped α-Fe$_2$O$_3$ thin films active for photoelectrochemical water splitting. Chem. Mater. 39 (38), 3803–3805.

Hua, Z., Dai, Z., Bai, X., Ye, Z., Wang, P., Gu, H., et al., 2015. Copper nanoparticles sensitized TiO$_2$ nanotube arrays electrode with enhanced photoelectrocatalytic activity for diclofenac degradation. Chem. Eng. J. 283, 514–523.

Julien, C., Massot, M., Baddour-Hadjean, R., Franger, S., Bach, S., Pereira-Ramos, J.P., 2003. Raman spectra of birnessite manganese dioxides. Solid State Ionics 159 (3–4), 345–356.

Kesselman, J.M., Lewis, N.S., Hoffmann, M.R., 1997. Photoelectrochemical degradation of 4-chlorocatechol at TiO$_2$ electrodes: comparison between sorption and photoreactivity. Environ. Sci. Technol. 31 (8), 2298–2302.

Kwon, K.D., Refson, K., Sposito, G., 2008. Defect-induced photoconductivity in layered manganese oxides: a density functional theory study. Phys. Rev. Lett. 100 (100), 1131–1137.

Lan, S., Cai, J., Qi, W., Pan, H., Su, Y., Lin, C., 2013. N-doped TiO$_2$ nanotube array photoelectrode for visible-light-induced photoelectrochemical and photoelectrocatalytic activities. Electrochim. Acta 108 (10), 525–531.

Leland, J.K., Bard, A.J., 1987. Photochemistry of colloidal semiconducting iron oxide polymorphs. J. Phys. Chem. 91 (19), 5076–5083.

Nakayama, M., Mai, N., Shamoto, M., Tanimoto, T., Tomono, K., Inoue, R., 2012. Cathodic synthesis of birnessite-type layered manganese oxides for electrocapacitive catalysis. J. Electrochem. Soc. 159 (8), A1176–A1182.

Nakayama, M., Shamoto, M., Kamimura, A., 2010. Surfactant-induced electrodeposition of layered manganese oxide with large interlayer space for catalytic oxidation of phenol. Chem. Mater. 22 (21), 5887–5894.

Neumann-Spallart, M., Shinde, S.S., Mahadik, M., Bhosale, C.H., 2013. Photoelectrochemical degradation of selected aromatic molecules. Electrochim. Acta 111 (6), 830–836.

Ohko, Y., 1997. Kinetics of photocatalytic reactions under extremely low-intensity UV illumination on titanium dioxide thin films. J. Phys. Chem. A. 101 (43), 8057–8062.

Philippidis, N., Sotiropoulos, S., Efstathiou, A., Poulios, I., 2009. Photoelectrocatalytic degradation of the insecticide imidacloprid using TiO$_2$/Ti electrodes. J. Photochem. Photobiol. A 204 (2), 129–136.

Pinaud, B.A., Chen, Z., Abram, D.N., Jaramillo, T.F., 2011. Thin films of sodium birnessite-type MnO$_2$: optical properties, electronic band structure, and solar photoelectrochemistry. J. Phys. Chem. C 115 (23), 11830–11838.

Sakai, N., Ebina, Y., Takada, K., Sakai, T., 2005. Photocurrent generation from semiconducting manganese oxide nanosheets in response to visible light. J. Phys. Chem. B 109 (19), 9651–9655.

Sherman, D.M., 2005. Electronic structures of iron(III) and manganese(IV) (hydr)oxide minerals: thermodynamics of photochemical reductive dissolution in aquatic environments. Geochim. Cosmochim. Acta 69 (69), 3249–3255.

Shinde, S.S., Bhosale, C.H., Rajpure, K.Y., 2012. Oxidative degradation of acid orange 7 using Ag-doped zinc oxide thin films. J. Photochem. Photobiol. B Biol. 117, 262–268.

Shinde, S.S., Bhosale, C.H., Rajpure, K.Y., 2013. Kinetic analysis of heterogeneous photocatalysis: role of hydroxyl radicals. Catal. Rev. Sci. Eng. 55 (1), 79–133.

Shinde, S.S., Sami, A., Lee, J.H., 2016. Sulfur mediated graphitic carbon nitride/S-Se-graphene as a metal-free hybrid photocatalyst for pollutant degradation and water splitting. Carbon 96, 929–936.

Spichiger-Ulmann, M., Augustynski, J., 1983. Aging effects in n-type semiconducting WO$_3$ films. J. Appl. Phys. 54 (10), 6061–6064.

Turchi, C.S., Ollis, D.F., 1990. Photocatalytic degradation of organic water contaminants: mechanisms involving hydroxyl radical attack. J. Catal. 122 (1), 178–192.

Ukrainczyk, L., 1992. Oxidation of phenol in acidic aqueous suspensions of manganese oxides. Clay Clay Miner. 773 (40), 157–166.

Wu, T.H., Cheng, I.C., Hsu, C.C., Chen, J.Z., 2015. UV photocurrent responses of ZnO and Mg ZnO/ZnO processed by atmospheric pressure plasma jets. J. Alloys Compd. 628, 68–74.

Yang, J., Chen, C., Ji, H., Ma, H., Zhao, J., 2005. Mechanism of TiO_2-assisted photocatalytic degradation of dyes under visible irradiation: photoelectrocatalytic study by TiO_2-film electrodes. J. Phys. Chem. B 109 (46), 21900–21907.

Yang, K., Pu, W., Tan, Y., Zhang, M., Yang, C., Zhang, J., 2014. Enhanced photoelectrocatalytic activity of Cr-doped TiO_2 nanotubes modified with polyaniline. Mater. Sci. Semicond. Process. 27, 777–784.

Yang, S., Liu, Y., Sun, C., 2006. Preparation of anatase TiO_2/Ti nanotube-like electrodes and their high photoelectrocatalytic activity for the degradation of PCP in aqueous solution. Appl. Catal. A Gen. 301 (2), 284–291.

Ye, Q., Lu, H., Zhao, J., Cheng, S., Kang, T., Wang, D., et al., 2014. A comparative investigation on catalytic oxidation of co, benzene, and toluene over birnessites derived from different routes. Appl. Surf. Sci. 317, 892–901.

Zaied, M., Chutet, E., Peulon, S., Bellakhal, N., Desmazières, B., Dachraoui, M., et al., 2011. Spontaneous oxidative degradation of indigo carmine by thin films of birnessite electrodeposited onto SnO_2. Appl. Catal. B Environ. 107 (1), 42–51.

Zhang, X., Lei, L., 2008. Preparation of photocatalytic Fe_2O_3–TiO_2 coatings in one step by metal organic chemical vapor deposition. Appl. Surf. Sci. 254 (8), 2406–2412.

Zhang, Z., Hossain, M.F., Takahashi, T., 2010. Self-assembled hematite (α-Fe_2O_3) nanotube arrays for photoelectrocatalytic degradation of azo dye under simulated solar light irradiation. Appl. Catal. B Environ. 95 (3), 423–429.

Zhang, Z., Shi, G., Fang, Y., Liang, L., Ding, H., Jin, L., 2007. Photoelectrocatalytic activity of highly ordered TiO_2 nanotube arrays electrode for azo dye degradation. Environ. Sci. Technol. 41 (17), 6259–6263.